

5/20/2014

An Introduction to the LS-DYNA[®] Smoothed Particle Galerkin Method for Severe Deformation and Failure Analyses in Solids

C. T. Wu^{1*}, Y. Guo¹ and W. Hu¹¹ Livermore Software Technology Corporation
7374 Las Positas Road, Livermore, CA 94550, USA

Abstract

This paper presents a new particle method in LS-DYNA for the severe deformation and failure analyses of solid mechanics problems. The new formulation is first established following a standard meshfree Galerkin approach for a solving of the partial differential equation of linear elastic problems. A smoothed displacement field is introduced to the Galerkin formulation and leads to a regularized smoothed strain approximation. The resultant smoothed/regularized strain formulation can be related to the residual-based stabilization method for the elimination of zero-energy modes in the conventional particle methods. The discretized system of equations are consistently derived within the meshfree Galerkin variational framework and integrated using a direct nodal integration scheme. The linear formulation is next extended to the large deformation and failure analyses of inelastic materials. In the severe deformation range, an adaptive Lagrangian or Eulerian kernel approach can be preformed to reset the reference configuration and maintain the injective deformation mapping at the particles. Several numerical benchmarks are provided to demonstrate the effectiveness and accuracy of the proposed method.

Keywords: particle; convex approximation; nodal integration; inelastic

1. Introduction

Meshfree, or particle methods, offer many numerical advantages over the conventional finite element and finite difference methods in modeling large deformation, moving discontinuity and immersed problems in solid and structural applications [1]. Those methods were also found to be very effective in reducing the volumetric locking and shear locking in the solid and structural analyses [3]. The earliest development in the meshfree methods was the Smoothed Particle Hydrodynamics (SPH) method. The foundation of the SPH method is the kernel estimate introduced by Monaghan [6]. In this method, partial differential equations are transformed into integral equations and the kernel estimate then provides the approximation to estimate the field variables at discrete particles. Since the functions are evaluated only at the particles, the use of a mesh is no longer required. The ability to handle severe deformations without the use of meshes in fluid-like motion allows the SPH method to be applied to problems that historically have been reserved for Eulerian approaches [7-8]. Nevertheless, a direct application of the SPH method to

* Corresponding author. Tel: +1 925-2454529; Fax: +1 925-4492507.
E-mail address: ctwu@lstc.com (C. T. Wu).

solid and structural analyses suffers from several numerical deficiencies, namely the lack of approximation consistency, tension instability, diffusion in material history information, presence of spurious or zero-energy modes and difficulty in enforcing the essential boundary conditions [9-10].

The Reproducing Kernel Particle method (RKPM) [10] introduced a correction function that restores the first-order consistency of the kernel approximation in the SPH method and improves the solution accuracy for finite domain problems. Tensile instability [12] is a major numerical defect in the SPH method that exhibits numerical fracture and artificial voids in the solid and structural applications. Tension instability was first identified by Sweigle *et al.* [13] in a Von Neumann stability analysis and was later found to be related to the Eulerian kernels used in the Lagrangian description of motion [14]. A byproduct of Eulerian kernels in SPH is the diffusion problem in tracking the material history information during the deformation. Although an adoption of Lagrangian kernels can be used to alleviate the tension instability and reduce the diffusion problem [15], it suffers excessively from the intrinsic defects of purely Lagrangian methods and limits the magnitude of distortions in the severe deformation analysis. The presence of spurious or zero-energy modes in SPH or other Galerkin-based meshfree methods is mainly due to the rank instability caused by the under-integration of the weak forms inherent in the central difference formula from the nodal integration. Several meshfree nodal integration methods [16] have been developed to eliminate the spurious zero or near-singular modes due to the rank instability using the direct nodal integration scheme. Chen *et al.* [18] proposed a Stabilized Conforming Nodal Integration (SCNI) method in which a strain smoothing scheme was introduced as a stabilization process for the nodal integration. A common feature of the SPH stress point and the SCNI methods is their integration of the discretized system of equations over the background, or integration, cells, thus limiting their ability to model severe deformation problems.

The robustness and accuracy of the meshfree or particle methods in the solid and structural analyses are also greatly affected by their numerical treatments of the boundary conditions. Since the Kronecker-delta property does not hold in the conventional meshfree approximations such as the SPH kernel approximation, Moving Least-squares (MLS) or Reproducing Kernel (RK) approximations, special techniques [3] are needed to impose the constraint and the essential boundary conditions in the meshfree methods. Alternatively, several convex approximations were introduced [20] to simplify the essential boundary condition treatment in the meshfree methods. Meshfree convex approximations guarantee the unique solution inside a convex hull with a minimum distributed data set and possess the Kronecker-delta property at the boundaries, therefore avoid any special treatment on the essential boundaries. It has been shown [21] that the meshfree convex approximation exhibits smaller lagging phase and amplitude errors than the meshfree non-convex approximation in a full-discretization of the wave equation. Several meshfree and meshfree-enriched Galerkin formulations [22] using the meshfree convex approximation have been presented for the analyses of immersed composites, rubber-like materials in large deformation, and multi-scale acoustic waves.

This paper presents an alternative particle formulation [10] that provides a stable and accurate solution for problems in the solid mechanics applications. Since the formulation is derived based on a smoothed displacement field within the meshfree Galerkin variational framework and the discretized system of equations are integrated at the particles, we refer this formulation as the Smoothed Particle Galerkin (SPG) method. The remainder of the paper is outlined as follows: In the next section, we define the boundary-value problem of the linear elasticity and formulate the meshfree Galerkin method. In Section 3, we present a Smoothed Particle Galerkin formulation and its strain regularization. In Section 4, the Smoothed Particle Galerkin formulation is

extended to the large deformation analysis of inelastic materials with the adaptive Lagrangian or Eulerian kernel approach. Section 5 describes the SPG explicit dynamic formulation. The LS-DYNA input format is also provided in the same section. Several numerical examples are presented in Section 6 to illustrate the accuracy and robustness of the method. Final remarks are drawn in Section 7.

2. Preliminaries

To better illustrate the fundamental concept of the present method, we first consider the static response of an elastic body under plain strain conditions. We assume the domain $\Omega \subset \mathbb{R}^2$ be a bounded polygon with the smooth boundary $\Gamma = \partial\Omega$. Also, let \mathbf{u} be the displacement and further assume that the Dirichlet boundary conditions are applied on Γ_D and the Neumann boundary conditions are prescribed on Γ_N . For a prescribed body force $\mathbf{f}(\mathbf{X}) \in L^2(\Omega)$, the governing equilibrium equation and boundary conditions are written as

$$\begin{aligned} -\nabla \cdot \boldsymbol{\sigma}(\mathbf{u}) &= \mathbf{f} \quad \text{in } \Omega \\ \mathbf{u} &= \mathbf{g} \quad \text{on } \Gamma_D \\ \boldsymbol{\sigma} \cdot \mathbf{n} &= \mathbf{t} \quad \text{on } \Gamma_N \end{aligned} \quad (\Gamma_D \cup \Gamma_N = \Gamma; \Gamma_D \cap \Gamma_N = \emptyset) \quad (1)$$

where \mathbf{g} is the prescribed displacement on Γ_D , \mathbf{t} is the prescribed traction, \mathbf{n} is the outward unit normal to the boundary Γ_N and $\nabla \cdot$ stands for the divergence operator. The infinitesimal strain tensor $\boldsymbol{\varepsilon}(\mathbf{u})$ is defined by

$$\boldsymbol{\varepsilon}(\mathbf{u}) = \frac{1}{2}(\nabla \mathbf{u} + \mathbf{u} \nabla) \equiv \nabla^s \mathbf{u} \quad (2)$$

where ∇ is the gradient operator. In the case of linear isotropic elasticity, the Cauchy stress tensor $\boldsymbol{\sigma}$ and strain tensor $\boldsymbol{\varepsilon}$ have the following relationship

$$\boldsymbol{\sigma} = \mathbf{C} : \boldsymbol{\varepsilon}(\mathbf{u}) = 2\mu \boldsymbol{\varepsilon}(\mathbf{u}) + \lambda \text{tr}(\boldsymbol{\varepsilon}(\mathbf{u})) \mathbf{I} \quad (3)$$

where \mathbf{C} is the fourth-order elasticity tensor and \mathbf{I} is the identity tensor. The positive constants μ and λ are the Lamé constants such that $\mu \in [\mu_1, \mu_2]$ with $0 < \mu_1 < \mu_2$ and $\lambda \in (0, \infty)$. The Lamé constants can be related to the Young's modulus E and the Poisson ratio ν by

$$\mu = \frac{E}{2(1+\nu)}, \quad \lambda = \frac{\nu E}{(1+\nu)(1-2\nu)} \quad (4)$$

The variational form of this problem is to find the displacement $\mathbf{u} \in \mathcal{V}^s = \{\mathbf{v} \in \mathbf{H}^1(\Omega) : \mathbf{v} = \mathbf{g} \text{ on } \Gamma_D\}$ such that for all $\delta \mathbf{u} \in \mathcal{V}$

$$\int_{\Omega} \delta(\nabla^s \mathbf{u}) : \mathbf{C} : (\nabla^s \mathbf{u}) d\Omega - \int_{\Omega} \delta \mathbf{u} \cdot \mathbf{f} d\Omega - \int_{\Gamma_N} \delta \mathbf{u} \cdot \mathbf{t} d\Gamma = 0 \quad (5)$$

where the space $\mathcal{V} = \mathbf{H}_0^1(\Omega)$ consists of the functions in the Sobolev space $\mathbf{H}^1(\Omega)$ which vanishes on the boundary in the sense of traces and is defined by

$$\mathcal{V}(\Omega) = \{\mathbf{v} : \mathbf{v} \in \mathbf{H}^1, \mathbf{v} = \mathbf{0} \text{ on } \Gamma_D\} \quad (6)$$

By the Lax-Milgram theorem, there exists a unique solution $\mathbf{u} \in V^g$ to the problem. Moreover, let $\mathbf{u} \in V^g \cap H^2 \{ \mathbf{f} \in L^2(\Omega), \mathbf{g} = \mathbf{w}_1|_{\Gamma_D}, \text{ where } \mathbf{w}_1 \in H^2(\Omega), \text{ and } \mathbf{t} = \mathbf{w}_2|_{\Gamma_N}, \text{ where } \mathbf{w}_2 \in H^1(\Omega) \}$, we have the following elliptic regularity estimate for the linear elasticity posed in a convex domain with a polygonal boundary:

$$\|\mathbf{u}\|_2 + \lambda \|\nabla \cdot \mathbf{u}\|_1 \leq C_1 (\|\mathbf{f}\|_0 + \|\mathbf{w}_1\|_2 + \|\mathbf{w}_2\|_1) \quad (7)$$

where $\|\cdot\|_m$ is the Sobolev norm of order m as defined in a standard way. The constant C_1 in Eq.(7) does not depend on λ and μ .

For simplicity, we assume the homogenous Dirichlet boundary conditions in the following derivation. The standard meshfree Galerkin method is then formulated on a finite dimensional subspace $V^h \subset V$ employing the variational formulation of Eq. (5) to find $\mathbf{u}^h \in V^h$ such that

$$\delta \Pi = \int_{\Omega} \delta(\nabla^s \mathbf{u}^h) : \mathbf{C} : (\nabla^s \mathbf{u}^h) d\Omega - \int_{\Omega} \delta \mathbf{u}^h \cdot \mathbf{f} d\Omega - \int_{\Gamma_N} \delta \mathbf{u}^h \cdot \mathbf{t} d\Gamma = 0 \quad \forall \delta \mathbf{u}^h \in V^h \quad (8)$$

3. A Smoothed Particle Galerkin Formulation for Linear Elasticity

This section describes the derivation of the smoothed particle Galerkin formulation for the analysis of linear elasticity problems using a direct nodal integration scheme. For a particle distribution noted by an index set $Z_I = \{\mathbf{X}_I\}_{I=1}^{NP}$, we approximate the displacement field using the meshfree approximation constructed by either the conventional meshfree approximation methods or the convex approximation methods to give

$$\mathbf{u}^h(\mathbf{X}) = \sum_{I=1}^{NP} \Psi_I(\mathbf{X}) \tilde{\mathbf{u}}_I \equiv \hat{\mathbf{u}}(\mathbf{X}) \quad \forall \mathbf{X} \in \Omega \quad (9)$$

where NP is the total number of particles, and $\Psi_I(\mathbf{X}), I=1, \dots, NP$ can be considered as the shape functions of the meshfree approximation for the displacement field $\mathbf{u}^h(\mathbf{X})$. With the meshfree shape functions, we can define the corresponding finite-dimensional approximation space to be $V^h = \text{span} \{ \Psi_I(\mathbf{X}) : I \in Z_I \text{ and } \mathbf{X} \in \Omega \}$. In general, $\tilde{\mathbf{u}}_I$ is not the particle displacement and is often referred to as the ‘‘generalized’’ displacement of particle I in the meshfree Galerkin method. Using Eq. (9), the particle displacement at particle I can be expressed by

$$\mathbf{u}^h(\mathbf{X}_I) = \sum_{J=1}^{NP} \Psi_J(\mathbf{X}_I) \tilde{\mathbf{u}}_J \equiv \hat{\mathbf{u}}_I \quad (10)$$

where $\mathbf{X}_I = (X_I, Y_I)$ is the nodal coordinate of particle I . If the meshfree shape functions $\Psi_I(\mathbf{X})$ are constructed using a convex approximation, then they have the Kronecker-delta property on the boundary, i.e. $\hat{\mathbf{u}}_I = \tilde{\mathbf{u}}_I$ for $\forall \mathbf{X}_I \in \Gamma$. In this study, the first-order convex approximation is constructed by the GMF method using the inverse tangent basis function and the cubic spline window function. Giving a convex hull $\text{Convex}(Z_I)$ of the node set $Z_I = \{\mathbf{X}_I, I = 1, \dots, NP\} \subset \mathfrak{R}^2$ defined by

$$\text{Convex}(Z_I) = \left\{ \sum_{I=1}^{NP} \alpha_I \mathbf{X}_I \mid \alpha_I \in \mathfrak{R}, \sum_{I=1}^{NP} \alpha_I = 1, \alpha_I \geq 0, \mathbf{X}_I \in Z_I \right\} \quad (11)$$

the GMF method is used to construct a convex approximation of a given (smooth) function $\mathbf{u}(\mathbf{X})$ in the form of Eq. (9) such that the shape function $\Psi_I : \text{Convex}(Z_I) \rightarrow \mathfrak{R}$ satisfies the following linear polynomial reproduction property

$$\sum_{I=1}^{NP} \Psi_I(\mathbf{X}) \mathbf{X}_I = \mathbf{X} \quad \forall \mathbf{X} \in \text{Convex}(Z_I) \quad (12)$$

With the meshfree convex approximation, we can also define a H_0^1 -conforming subspace for the approximation of the displacement field to be $\mathbf{V}^h := \text{span} \left\{ \Psi_I \mid (\text{supp } \Psi_I)^0 \subset \Omega, I \in Z_I \right\}$. An evaluation of the weak form in Eq. (8) using the meshfree approximation and the direct nodal integration scheme leads to the spurious, or zero-energy, modes. This is a consequence of the fact that the field variables and their derivatives are calculated at the same points such that an alternating field variable has a zero gradient at the particles [25]. The almost vanishing first derivatives at the nodes result in a discrete weak form that does not adequately reflect the strain energy and its contribution to the stiffness matrix is severely underestimated [16]. In order to eliminate the presence of the spurious or zero-energy modes caused by the direct nodal integration scheme, the smoothed particle Galerkin method introduces a smoothing of the displacement field defined by

$$\bar{\mathbf{u}}(\mathbf{X}) = \int_{\Omega} \tilde{\Psi}(\mathbf{Y}; \mathbf{X}) \hat{\mathbf{u}}(\mathbf{Y}) d\Omega \quad (13)$$

where \mathbf{Y} denotes the position of the infinitesimal volume $d\Omega$. The discrete form of Eq. (13) becomes

$$\bar{\mathbf{u}}_I = \sum_{J=1}^{NP} \tilde{\Psi}_J(\mathbf{X}_I) \hat{\mathbf{u}}_J \quad (14)$$

where $\tilde{\Psi}_J(\mathbf{X}_I)$, $J=1, \dots, NP$ are the displacement smoothing functions for particle I . It is assumed that the displacement smoothing functions $\tilde{\Psi}$ also satisfy the linear polynomial reproduction condition. In another words, the smoothed displacement field $\bar{\mathbf{u}}(\mathbf{X})$ equals to $\hat{\mathbf{u}}(\mathbf{X})$ for homogeneous displacement states. For a sufficiently smoothed displacement field $\hat{\mathbf{u}}(\mathbf{X})$, the integral form in Eq.(13) can be expressed in terms of the gradients of $\hat{\mathbf{u}}(\mathbf{X})$ by expanding $\hat{\mathbf{u}}(\mathbf{X})$ into a Taylor series to yield

$$\hat{\mathbf{u}}(\mathbf{Y}) = \hat{\mathbf{u}}(\mathbf{X}) + \nabla \hat{\mathbf{u}}(\mathbf{X}) \cdot (\mathbf{Y} - \mathbf{X}) + \frac{1}{2!} \nabla^{(2)} \hat{\mathbf{u}}(\mathbf{X}) \cdot^{(2)} (\mathbf{Y} - \mathbf{X})^{(2)} + \frac{1}{3!} \nabla^{(3)} \hat{\mathbf{u}}(\mathbf{X}) \cdot^{(3)} (\mathbf{Y} - \mathbf{X})^{(3)} + \dots \quad (15)$$

where $\nabla^{(n)}$ denotes the n th-order gradient operator and $\cdot^{(n)}$ denotes the n th-order inner product. The symbol $(\xi)^{(n)}$ designates the n factor dyadic product $(\xi)(\xi) \dots (\xi)$ for a vector ξ . Substituting Eq.(15) into Eq.(13) leads to the following smoothed displacement field in terms of the gradients

$$\begin{aligned} \bar{\mathbf{u}}(\mathbf{X}) &= \int_{\Omega} \tilde{\Psi}(\mathbf{Y}; \mathbf{X}) \hat{\mathbf{u}}(\mathbf{X}) d\Omega + \int_{\Omega} \tilde{\Psi}(\mathbf{Y}; \mathbf{X}) \nabla \hat{\mathbf{u}}(\mathbf{X}) \cdot (\mathbf{Y} - \mathbf{X}) d\Omega \\ &+ \frac{1}{2!} \int_{\Omega} \tilde{\Psi}(\mathbf{Y}; \mathbf{X}) \nabla^{(2)} \hat{\mathbf{u}}(\mathbf{X}) \cdot^{(2)} (\mathbf{Y} - \mathbf{X})^{(2)} d\Omega \\ &+ \frac{1}{3!} \int_{\Omega} \tilde{\Psi}(\mathbf{Y}; \mathbf{X}) \nabla^{(3)} \hat{\mathbf{u}}(\mathbf{X}) \cdot^{(3)} (\mathbf{Y} - \mathbf{X})^{(3)} d\Omega + O(\|\mathbf{Y} - \mathbf{X}\|^{(4)}) \end{aligned} \quad (16)$$

Truncating the Taylor series in Eq.(16) after the quadratic term and using the linear polynomial reproduction condition of the displacement smoothing functions $\tilde{\Psi}$ leads to

$$\begin{aligned}
\bar{\mathbf{u}}(\mathbf{X}) &\approx \int_{\Omega} \tilde{\Psi}(\mathbf{Y}; \mathbf{X}) \hat{\mathbf{u}}(\mathbf{X}) d\Omega + \int_{\Omega} \tilde{\Psi}(\mathbf{Y}; \mathbf{X}) \nabla \hat{\mathbf{u}}(\mathbf{X}) \cdot (\mathbf{Y} - \mathbf{X}) d\Omega \\
&\quad + \frac{1}{2!} \int_{\Omega} \tilde{\Psi}(\mathbf{Y}; \mathbf{X}) \nabla^{(2)} \hat{\mathbf{u}}(\mathbf{X}) \cdot^{(2)} (\mathbf{Y} - \mathbf{X})^{(2)} d\Omega \\
&= \hat{\mathbf{u}}(\mathbf{X}) \int_{\Omega} \tilde{\Psi}(\mathbf{Y}; \mathbf{X}) d\Omega + \nabla \hat{\mathbf{u}}(\mathbf{X}) \left(\int_{\Omega} \tilde{\Psi}(\mathbf{Y}; \mathbf{X}) (\mathbf{Y}) d\Omega - \mathbf{X} \int_{\Omega} \tilde{\Psi}(\mathbf{Y}; \mathbf{X}) d\Omega \right) \\
&\quad + \nabla^{(2)} \hat{\mathbf{u}}(\mathbf{X}) \cdot^{(2)} \left(\frac{1}{2!} \int_{\Omega} \tilde{\Psi}(\mathbf{Y}; \mathbf{X}) (\mathbf{Y} - \mathbf{X})^{(2)} d\Omega \right) \\
&= \hat{\mathbf{u}}(\mathbf{X}) \int_{\Omega} \tilde{\Psi}(\mathbf{Y}; \mathbf{X}) d\Omega + \nabla^{(2)} \hat{\mathbf{u}}(\mathbf{X}) \cdot^{(2)} \left(\frac{1}{2!} \int_{\Omega} \tilde{\Psi}(\mathbf{Y}; \mathbf{X}) (\mathbf{Y} - \mathbf{X})^{(2)} d\Omega \right) \\
&= \hat{\mathbf{u}}(\mathbf{X}) + \nabla^{(2)} \hat{\mathbf{u}}(\mathbf{X}) \cdot^{(2)} \boldsymbol{\eta}(\mathbf{X})
\end{aligned} \tag{17}$$

with $\boldsymbol{\eta}(\mathbf{X}) = \frac{1}{2!} \int_{\Omega} \tilde{\Psi}(\mathbf{Y}; \mathbf{X}) (\mathbf{Y} - \mathbf{X})^{(2)} d\Omega$ defines the position dependent coefficients. In a nodal integration, $|\boldsymbol{\eta}(\mathbf{X}_I)| \propto h^2$ that is proportional to a length squared where h denotes a characteristic length scale of the discretization. Note that with the convex approximation, we have $\boldsymbol{\eta}(\mathbf{X}_I) = \mathbf{0}$ and $\bar{\mathbf{u}}(\mathbf{X}_I) = \hat{\mathbf{u}}(\mathbf{X}_I)$ for \mathbf{X}_I on Γ . A modified weak form is obtained by neglecting the higher-order gradient terms in strains to find $\hat{\mathbf{u}} \in \mathcal{V}^h$, such that

$$a^h(\hat{\mathbf{u}}, \delta \hat{\mathbf{u}}) = l(\delta \hat{\mathbf{u}}) \quad \forall \delta \hat{\mathbf{u}} \in \mathcal{V}^h \tag{18}$$

where

$$\begin{aligned}
a^h(\hat{\mathbf{u}}, \delta \hat{\mathbf{u}}) &= \int_{\Omega} \delta(\nabla^s \hat{\mathbf{u}}) : \mathbf{C} : (\nabla^s \hat{\mathbf{u}}) d\Omega + \int_{\Omega} \delta(\bar{\nabla}^{(2)} \hat{\mathbf{u}}) : \mathbf{C} : (\bar{\nabla}^{(2)} \hat{\mathbf{u}}) d\Omega \\
&= a_{stan}^h(\hat{\mathbf{u}}, \delta \hat{\mathbf{u}}) + a_{stab}^h(\hat{\mathbf{u}}, \delta \hat{\mathbf{u}})
\end{aligned} \tag{19}$$

$$l(\delta \hat{\mathbf{u}}) = \int_{\Omega} \delta \hat{\mathbf{u}} \cdot \mathbf{f} d\Omega + \int_{\Gamma_N} \delta \hat{\mathbf{u}} \cdot \mathbf{t} d\Gamma - \int_{\Omega} (\delta \bar{\nabla}^{(2)} \hat{\mathbf{u}} : \boldsymbol{\eta}) \cdot \mathbf{f} d\Omega \tag{20}$$

where a_{stan}^h is the standard bilinear form defined in Eq. (8) and

$$\begin{aligned}
a_{stab}^h(\hat{\mathbf{u}}, \delta \hat{\mathbf{u}}) &= \int_{\Omega} \delta(\bar{\nabla}^{(2)} \hat{\mathbf{u}}) : \mathbf{C} : (\bar{\nabla}^{(2)} \hat{\mathbf{u}}) d\Omega \\
\bar{\nabla}^{(2)} \hat{\mathbf{u}} &= \frac{1}{2} (\nabla \boldsymbol{\eta} : \hat{\mathbf{u}} \nabla^{(2)} + \nabla^{(2)} \hat{\mathbf{u}} : \boldsymbol{\eta} \nabla)
\end{aligned} \tag{21}$$

defines the stabilized bilinear form which corresponds to the variation of the stabilized potential energy. The stabilization terms containing the first derivatives of the displacements are also omitted in Eq.(21) by considering their zero gradients at the particles. In the standard isotropic linear elastic case, coercivity of the bilinear form $a^h(\cdot, \cdot)$ on $\mathcal{V}^h \times \mathcal{V}^h$ follows immediately from one of the Korn's inequalities to give

$$\begin{aligned}
\|\hat{\mathbf{u}}\|_1^2 &\leq c_1 \|\nabla^s \hat{\mathbf{u}}\|_0^2 \leq c_1 \left(\|\nabla^s \hat{\mathbf{u}}\|_0^2 + \|\bar{\nabla}^{(2)} \hat{\mathbf{u}}\|_0^2 \right) \\
&\leq \frac{c_1}{\gamma_{\min}(\mathbf{C})} \left(a_{stan}^h(\hat{\mathbf{u}}, \hat{\mathbf{u}}) + a_{stab}^h(\hat{\mathbf{u}}, \hat{\mathbf{u}}) \right) \\
&= c_2 a^h(\hat{\mathbf{u}}, \hat{\mathbf{u}}), \quad c_1, c_2 > 0, \quad \hat{\mathbf{u}} \in V^h
\end{aligned} \tag{22}$$

where γ_{\min} is the smallest eigenvalue of \mathbf{C} . In other words, the stabilization term can be considered to enhance the coercivity of the formulation in the particle integration method. Using the Cauchy-Schwarz inequality and the first-order meshfree interpolation property [20] for the displacement smoothing function $\tilde{\Psi}$, $a^h(\cdot, \cdot)$ also can be bounded by

$$\begin{aligned}
|a^h(\hat{\mathbf{u}}, \hat{\mathbf{v}})| &\leq \int_{\Omega} |(\nabla^s \hat{\mathbf{u}}) : \mathbf{C} : (\nabla^s \hat{\mathbf{v}})| d\Omega + \int_{\Omega} |(\bar{\nabla}^{(2)} \hat{\mathbf{u}}) : \mathbf{C} : (\bar{\nabla}^{(2)} \hat{\mathbf{v}})| d\Omega \\
&\leq \gamma_{\max}(\mathbf{C}) \left\{ \left(\int_{\Omega} \|\hat{\boldsymbol{\varepsilon}}(\hat{\mathbf{u}})\|_0^2 d\Omega \right)^{1/2} + \left(\int_{\Omega} \|\hat{\boldsymbol{\varepsilon}}(\hat{\mathbf{v}})\|_0^2 d\Omega \right)^{1/2} \right. \\
&\quad \left. + c_3 \left(\int_{\Omega} \|h \nabla \hat{\boldsymbol{\varepsilon}}(\hat{\mathbf{u}})\|_0^2 d\Omega \right)^{1/2} + \left(\int_{\Omega} \|h \nabla \hat{\boldsymbol{\varepsilon}}(\hat{\mathbf{v}})\|_0^2 d\Omega \right)^{1/2} \right\} \\
&\leq \gamma_{\max}(\mathbf{C}) c_4 \{ \|\hat{\mathbf{u}}\|_1 \|\hat{\mathbf{v}}\|_1 \} \leq c_5 \|\hat{\mathbf{u}}\|_1 \|\hat{\mathbf{v}}\|_1, \quad c_3, c_4, c_5 > 0 \quad \forall \hat{\mathbf{u}}, \hat{\mathbf{v}} \in V^h
\end{aligned} \tag{23}$$

where γ_{\max} is the largest eigenvalue of \mathbf{C} . The third inequality is obtained using a simple triangle inequality for the strain component of norm $\|\hat{\boldsymbol{\varepsilon}}(\hat{\mathbf{u}})\|_0$ defined in L^2 space [22]. Since Eq. (21) includes non-zero second derivatives of the displacements, it serves as a stabilization term and appears like the residual-based stabilization method [16] for the nodal integration in the Element-Free Galerkin method. The numerical evaluation of Eq. (21) using a direct nodal integration results in a symmetric stiffness matrix. Compared to the residual-based stabilization method, the stabilization parameter in Eq. (21) is derived in a consistent manner without additional prescription of its value. However, the integration of Eq. (21) involves the second derivatives and is expensive for the assembly of linear systems in multi-dimensional problems. In this study, an alternative way to implement the smoothed displacement field in Eq. (8) without the involvement of second-order derivatives in the shape functions is introduced. This is to use the integral form in Eq. (13) instead of the gradient form in Eq. (17). By substituting Eq. (10) into Eq.(14), we have the discrete smoothed displacement field evaluated at the particles by

$$\begin{aligned}
\bar{\mathbf{u}}_I &= \sum_{J=1}^{NP} \tilde{\Psi}_J(\mathbf{X}_I) \hat{\mathbf{u}}_J = \sum_{J=1}^{NP} \tilde{\Psi}_J(\mathbf{X}_I) \sum_{K=1}^{NP} \Psi_K(\mathbf{X}_J) \tilde{\mathbf{u}}_K = \sum_{K=1}^{NP} \sum_{J=1}^{NP} \Psi_K(\mathbf{X}_J) \tilde{\Psi}_J(\mathbf{X}_I) \tilde{\mathbf{u}}_K \\
&= \sum_{K=1}^{NP} \phi_K(\mathbf{X}_I) \tilde{\mathbf{u}}_K
\end{aligned} \tag{24}$$

where the smoothed meshfree shape function $\phi_K(\mathbf{X}_I)$ is defined by

$$\phi_K(\mathbf{X}_I) := \sum_{J=1}^{NP} \Psi_K(\mathbf{X}_J) \tilde{\Psi}_J(\mathbf{X}_I) \tag{25}$$

Now the relationships between the different nodal position systems can be defined through Eqs. (10), (14) and (24), and are shown in Figure 1.

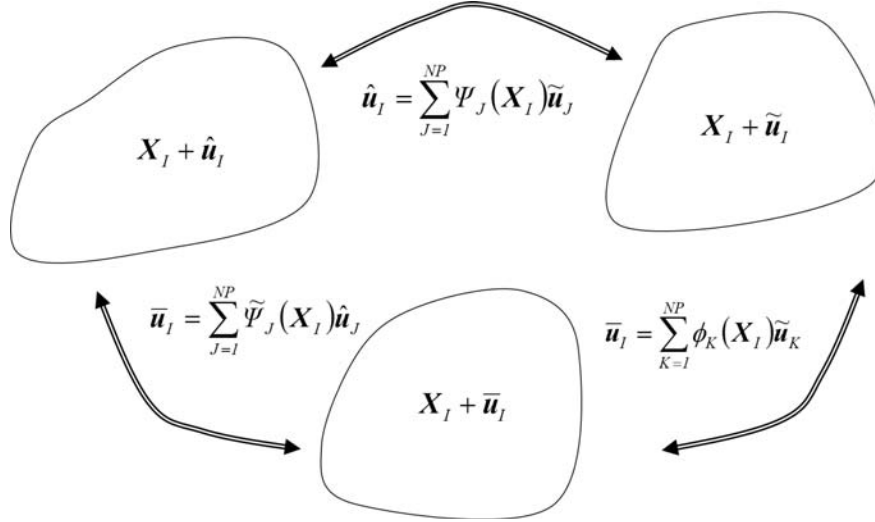


Figure 1: The relationships between different nodal position systems.

The smoothed meshfree shape function constructed by the meshfree convex approximation continues to satisfy the Kronecker-delta property on the boundary,

$$\phi_K(\mathbf{X}_I) = \sum_{J=1}^{NP} \Psi_K(\mathbf{X}_J) \tilde{\Psi}_J(\mathbf{X}_I) = \delta_{KI} \quad \forall \mathbf{X}_K \in \Gamma_g \quad (26)$$

Using Eq. (9), we have the admissible test functions for the variation equation obtained by

$$\delta \mathbf{u}^h(\mathbf{X}) = \sum_{I=1}^{NP} \Psi_I(\mathbf{X}) \delta \tilde{\mathbf{u}}_I \quad (27)$$

By introducing the displacement and strain approximations into Eq. (8), the discrete governing equation is integrated using a direct nodal integration to give

$$\delta \tilde{\mathbf{U}}^T \mathbf{K} \tilde{\mathbf{U}} = \delta \tilde{\mathbf{U}}^T \mathbf{f}^{ext} \quad (28)$$

$$\mathbf{K}_{IJ} = \int \mathbf{B}_I^T \mathbf{C} \mathbf{B}_J d\Omega = \sum_{K=1}^{NP} \mathbf{B}_I^T(\mathbf{X}_K) \mathbf{C} \mathbf{B}_J(\mathbf{X}_K) V_K^0 \quad (29)$$

$$\mathbf{f}_I^{ext} = \int_{\Omega} \Psi_I \mathbf{f} d\Omega + \int_{\Gamma_N} \Psi_I \mathbf{t} d\Gamma = \sum_{K=1}^{NP} \Psi_I(\mathbf{X}_K) \mathbf{f}(\mathbf{X}_K) V_K^0 + \sum_{K=1}^{NB} \Psi_I(\mathbf{X}_K) \mathbf{f}(\mathbf{X}_K) L_K \quad (30)$$

where V_K^0 denotes the initial volume of particle K . In Eq. (30) NB denotes the number of boundary nodes and L_k is the length associated with the boundary particle along the global boundary. To explore the concept of the method as well as to improve computational efficiency, we simply consider $\tilde{\Psi}_I(\mathbf{X}) = \Psi_I(\mathbf{X})$ in this study. From Eq. (14), we have

$$\bar{\mathbf{u}}_I = \sum_{K=1}^{NP} \Psi_K(\mathbf{X}_J) \sum_{J=1}^{NP} \Psi_J(\mathbf{X}_I) \tilde{\mathbf{u}}_K = \sum_{K=1}^{NP} \phi_K(\mathbf{X}_I) \tilde{\mathbf{u}}_K \quad (31)$$

or in matrix form

$$\bar{\mathbf{U}} = \mathbf{A} \tilde{\mathbf{U}} \quad \text{or} \quad \tilde{\mathbf{U}} = \mathbf{A}^{-1} \bar{\mathbf{U}} \quad (32)$$

where vector $\tilde{\mathbf{U}} = [\tilde{\mathbf{u}}_1, \tilde{\mathbf{u}}_2, \dots, \tilde{\mathbf{u}}_{NP}]$ contains the problem unknowns for the generalized nodal displacements. \mathbf{A} is a transformation matrix defined by

$$\mathbf{A}_{IJ} = \phi_J(\mathbf{X}_I) \mathbf{I} = \sum_{K=1}^{NP} \Psi_K(\mathbf{X}_I) \Psi_J(\mathbf{X}_K) \mathbf{I} \quad (33)$$

Substituting Eq. (32) into the variation form of Eq. (28) leads to the following discrete equation to be solved for the linear elastic analysis

$$\mathbf{A}^{-T} \mathbf{K} \mathbf{A}^{-1} \bar{\mathbf{U}} = \mathbf{A}^{-T} \mathbf{f}^{ext} \quad (34)$$

or equivalently

$$\mathbf{A}^{-T} \mathbf{K} \tilde{\mathbf{U}} = \mathbf{A}^{-T} \mathbf{f}^{ext} \quad (35)$$

4. Large Deformation Analysis for Inelastic Material and Adaptive Lagrangian/Eulerian Kernel Approach

The smoothed meshfree Galerkin formulation presented in the previous section is now extended to the nonlinear analysis of plastic materials. In light of the rate constitutive equations and the derivatives with respect to the spatial coordinates, it is advantageous to use the variational formulation of the equation of motion in terms of the updated Lagrangian formulation in the following derivation.

In a quasi-static problem, the variational formulation of the updated Lagrangian formulation with reference to the current configuration Ω_x is expressed in an index form by

$$\delta \Pi = \int_{\Omega_x} \delta \varepsilon_{ij} \sigma_{ij} d\Omega - \int_{\Omega_x} \delta u_i f_i d\Omega - \int_{\Gamma_N} \delta u_i t_i d\Gamma = 0 \quad (36)$$

where σ_{ij} is the Cauchy stress defined at the current configuration. We also have $x_i = X_i + u_i$ that relates the spatial coordinate \mathbf{x} to the reference coordinate \mathbf{X} . Linearizing of Eq. (36) leads to the iterative equations

$$\Delta \delta \Pi = \int_{\Omega_x} \delta \varepsilon_{ij} C_{ijkl} \Delta \varepsilon_{kl} d\Omega + \int_{\Omega_x} \delta u_{i,j} T_{ijkl} \Delta u_{k,l} d\Omega - \int_{\Omega_x} \delta u_i \Delta f_i d\Omega - \int_{\Gamma_N} \delta u_i \Delta t_i d\Gamma \quad (37)$$

where

$$C_{ijkl} = C_{ijkl}^{alg} - C_{ijkl}^* \quad (38)$$

$$C_{ijkl}^* = -\sigma_{jl} \delta_{ik} + \frac{1}{2} (\sigma_{il} \delta_{jk} + \sigma_{jl} \delta_{ik} + \sigma_{ik} \delta_{jl} + \sigma_{jk} \delta_{il}) \quad (39)$$

$$T_{ijkl} = \delta_{ik} \sigma_{jl} \quad (40)$$

C_{ijkl} is the material tangent response tensor, C_{ijkl}^{alg} is the algorithmic tangent response tensor for the infinitesimal plasticity. Substituting the discrete meshfree approximation in Eq. (24) and its variation into Eq. (37) leads to the discrete iterative equation given by

$$\delta \tilde{\mathbf{U}}^T \mathbf{K}_{n+1}^v (\Delta \tilde{\mathbf{U}})_{n+1}^{v+1} = \delta \tilde{\mathbf{U}}^T \mathbf{R}_{n+1}^v \quad (41)$$

The notation $(\bullet)_{n+1}^v$ represents the function to be computed in the v -th iteration during $(n+1)$ th time incremental step. Using Eq. (32), the discrete iterative equation can be written in the smoothed nodal position system as in the linear analysis to yield

$$\mathbf{A}^{-T} \mathbf{K}_{n+1}^v \mathbf{A}^{-1} (\Delta \bar{\mathbf{U}})_{n+1}^{v+1} = \mathbf{A}^{-T} \mathbf{R}_{n+1}^v \quad (42)$$

or equivalently

$$\mathbf{A}^{-T} \mathbf{K}_{n+1}^v (\Delta \tilde{\mathbf{U}})_{n+1}^{v+1} = \mathbf{A}^{-T} \mathbf{R}_{n+1}^v \quad (43)$$

As Lagrangian simulation proceeds, an adaptive Lagrangian/Eulerian kernel scheme is performed frequently to avoid the negative Jacobian in the Lagrangian calculation. In each adaptive step material quantities are computed at the particles without the usage of any background cells. Since the adaptive Lagrangian/Eulerian kernel approach does not involve remeshing and the particle computation is evaluated node-wisely, the material quantities at all particles are maintained in the Lagrangian setting and thus require no remap procedures. If we denote the variables before and after each adaptive time step to be superscripted with “-“and “+” respectively, the derivatives of the material meshfree shape functions with respect to the spatial coordinates right before $(k+1)$ -th adaptive time step can be expressed by

$$\Psi_{li}^- (\mathbf{x}^{k+1}) = \frac{\partial \Psi_l^- (\mathbf{x}^{k+1})}{\partial x_i^{k+1}} = \frac{\partial \Psi_l^- (\mathbf{x}^{k+1})}{\partial x_j^k} \frac{\partial x_j^k}{\partial x_j^{k+1}} = \frac{\partial \Psi_l^-}{\partial x_j^k} f_{ji}^{k-1} \quad (44)$$

where $f_{ji}^{k-1} = \frac{\partial x_j^k}{\partial x_i^{k+1}}$ defines the inverse of the incremental deformation gradient from k -th adaptive time step. At $(k+1)$ -th adaptive time step, the new derivatives of the material meshfree shape functions becomes

$$\Psi_{li}^+ (\mathbf{x}^{k+1}) = \frac{\partial \Psi_l^+ (\mathbf{x}^{k+1})}{\partial x_i} \quad (45)$$

5. Explicit Dynamic Formulation and LS-DYNA Input Format

5.1 Explicit dynamic formulation

The explicit dynamic version of the smoothed particle Galerkin formulation can be easily obtained by considering the inertial effect and following the previous quasi-static derivation to yield

$$\mathbf{A}^{-T} \mathbf{M} \mathbf{A}^{-1} \ddot{\mathbf{U}} = \mathbf{A}^{-T} (\mathbf{f}^{ext} - \mathbf{f}^{int}) \quad (46)$$

or equivalently

$$\mathbf{A}^{-T} \mathbf{M} \ddot{\mathbf{U}} = \mathbf{A}^{-T} (\mathbf{f}^{ext} - \mathbf{f}^{int}) \quad (47)$$

where $\ddot{\bar{U}}$ and $\ddot{\tilde{U}}$ contain the vector of particle accelerations evaluated in the smoothed nodal position system and generalized nodal position system, respectively. \mathbf{M} is the consistent mass matrix given by

$$\mathbf{M}_{IJ} = \sum_{N=1}^{NP} \rho_0 \Psi_I(\mathbf{X}_N) \Psi_J(\mathbf{X}_N) V_N^0 \mathbf{I} \quad (48)$$

where ρ_0 is the initial density. Eq. (46) also can be rewritten as

$$\bar{\mathbf{M}} \ddot{\tilde{U}} = \mathbf{A}^{-T} (\mathbf{f}^{ext} - \mathbf{f}^{int}) \quad (49)$$

with $\bar{\mathbf{M}} = \mathbf{A}^{-T} \mathbf{M} \mathbf{A}^{-1}$ defines a smoothed consist mass matrix. In an explicit dynamic analysis, a row-sum mass matrix is usually considered which is only computed once without involving the matrix inversion at each time step. The smoothed consist mass matrix is now replaced by the row-sum mass matrix $\bar{\mathbf{M}}^{RS}$ to give

$$\bar{\mathbf{M}}_I^{RS} = \sum_J \bar{\mathbf{M}}_{IJ} = \sum_J \mathbf{A}_{IK}^{-T} \mathbf{M}_{KM} \mathbf{A}_{ML}^{-1} \quad (50)$$

Since no remap procedures are considered in the adaptive Lagrangian kernel scheme, the particle mass is taken to be the same during the explicit dynamics analysis. The current particle volume required for the calculation of the internal force is updated according to the continuity equation given by

$$V_I = \frac{\rho_0}{\rho_I} V_I^0 \quad (51)$$

$$\frac{d\rho_I}{dt} = -\rho_I \nabla \cdot (\dot{\tilde{\mathbf{u}}}_I) = -\rho_I \sum_{J=1}^{NP} \dot{\tilde{\mathbf{u}}}_J \cdot \Psi_{J,x}(\mathbf{x}_I) \quad (52)$$

5.2 LS-DYNA input keyword

The new particle formulation is assigned an element type of 47 and can be accessed with an option of `_SPG` in the `*SECTION_SOLID` keyword card. It is implemented in such a way that one can easily take a finite element model and change some parts into SPG particles.

The input format is as follows:

`*SECTION_SOLID{ _SPG }`

Card1 1 2 3 4 5 6 7 8

Variable	SECID	ELFORM	AET						
Type	I	I	I						
Default									

The SPG method is selected by setting ELFORM to 47, and two optional input cards are defined to obtain additional input parameters from the user:

Card2	1	2	3	4	5	6	7	8
Variable	DX	DY	DZ	ISPLINE	IDISC	LSCALE	SMSTEP	SWTIME
Type	F	F	F	I	I	F	I	F
Default	1.5	1.5	1.5	0	0			
Card3	1	2	3	4	5	6	7	8
Variable	Others							
Type	I							
Default	0							

The variables are described as below:

<u>VARIABLE</u>	<u>DESCRIPTION</u>
SECID	Section ID.
ELFORM	Element formulation options. Set to 47 to active SPG method.
DX, DY, DZ	Normalized dilation parameters of the kernel functions in X, Y and Z directions.
ISPLINE	Option for kernel functions. EQ.0: Cubic spline function (default). EQ.1: Quadratic spline function. EQ.2: Cubic spline function with circular shape.
IDISC	Type of discretization. EQ.0: Moving least-square (default). EQ.1: Convex approximation.
LSCALE	Length scale for displacement regularization.
SMSTEP	Interval of time steps to conduct displacement regularization.
SWTIME	Time to switch from adaptive Lagrangian kernel to Eulerian kernel.
Others	Cards 3 leaves to further developments in material failure/damage analyses.

For the full description of the keyword *SECTION_SOLID, please refer to the LS-DYNA keyword users' manual.

6. Numerical Examples

6.1 Implicit analysis for radial bushing problem

This example is analyzed to identify the applicability of the proposed method to highly constrained problem using implicit version of SPG method. The radial metal bushing model in plain strain condition, as shown in Fig. 2, is studied, where the outer surface is fixed, and the inner surface sticks with an un-deformed core moving along vertical direction. The strain-

hardening elastic-plastic material properties of the workpiece are: Young's modulus $E=2.0 \times 10^6$, Poisson's ratio $\nu=0.3$, and an isotropic hardening rule $\sigma_y(\bar{\epsilon}^p) = \sigma_y^0 (1 + \alpha \bar{\epsilon}^p)^\beta$ with coefficients $\sigma_y^0 = 1.0 \times 10^3$, $\alpha = 2.0 \times 10^4$ and $\beta = 0.1$. $\bar{\epsilon}^p$ denotes the effective plastic strain and $\sigma_y(\bar{\epsilon}^p)$ is the flow stress which is a scalar and increases monotonically with the effective plastic strain. Since the convex approximation result agrees well with the MLS approximation result, only MLS approximation result is reported in this example. As comparison, we also provide the results using two well-established nodal integration methods. A list of abbreviations for those methods along with their brief description is given in Table 1. Unless otherwise specified, a normalized nodal support size of 2.0 is considered in the example. A dimensionless unit system is also adopted in this paper for convenience.

Table 1: Three nodal integration methods adopted in the numerical comparison

Name	Description
DNI(MLS)	MLS approximation with direct nodal integration
SCNI(MLS)	MLS approximation with stabilized conforming nodal integration
SPG(MLS)	MLS approximation with present formulation

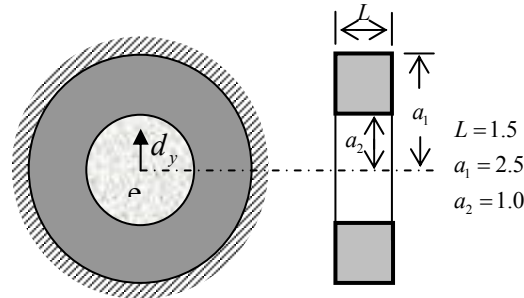


Figure 2: Radial bushing model.

The comparison of load-displacement curves using a discretization of 168 nodes is plotted in Fig. 3. In this highly constrained problem, the SPG result matches with DNI result very well. In contrast, the SCNI method generates a solution that is softer than the others in the large deformation range. The soft force response in SCNI result is partially due to the characteristic of upper bound solution using SCNI integration scheme and coarse discretization. The unstable low-energy modes observed in the deformation as shown in Fig. 4 can also be regarded as the causes to the soft force response in SCNI method. The superior performance of the present SPG method can be demonstrated in the smoothness of displacement and effective plastic strain fields as depicted in Fig 5.

Fig.6 provides the convergence study in this nonlinear analysis using SPG (MLS) method. It is shown in Fig. 6 that SPG (MLS) method provides a lower bound solution and suggests a convergence of reaction force as model is continuously refined.

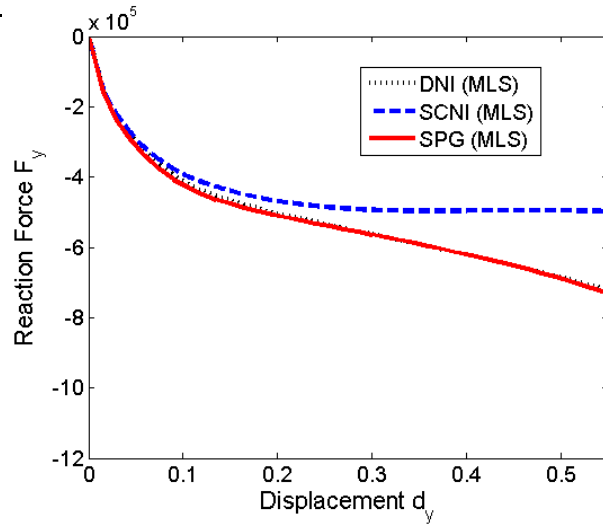


Fig. 3: Comparison of force-displacement curves in the Radial bushing problem.

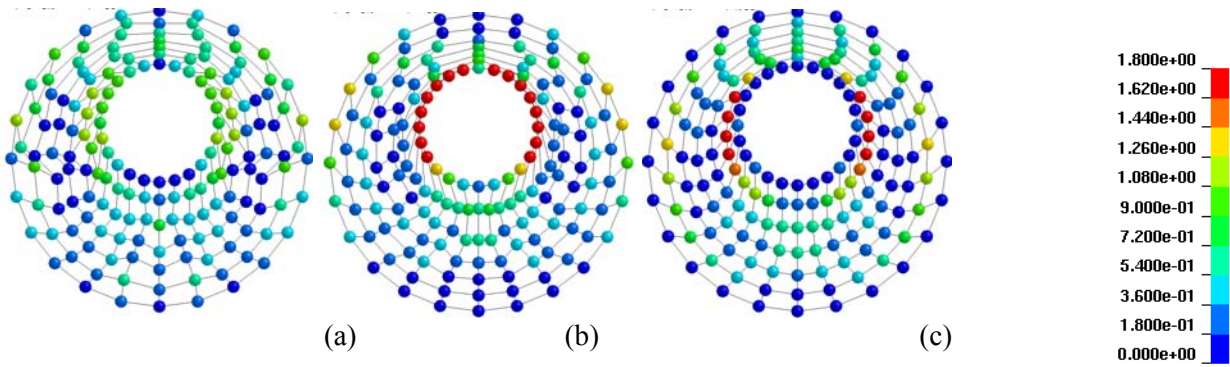


Fig. 4: Comparison of deformation plots with effective plastic strain results at $d_y=0.6$: (a) DNI (MLS) method, (b) SCNI (MLS) method, and (c) SPG (MLS) method.

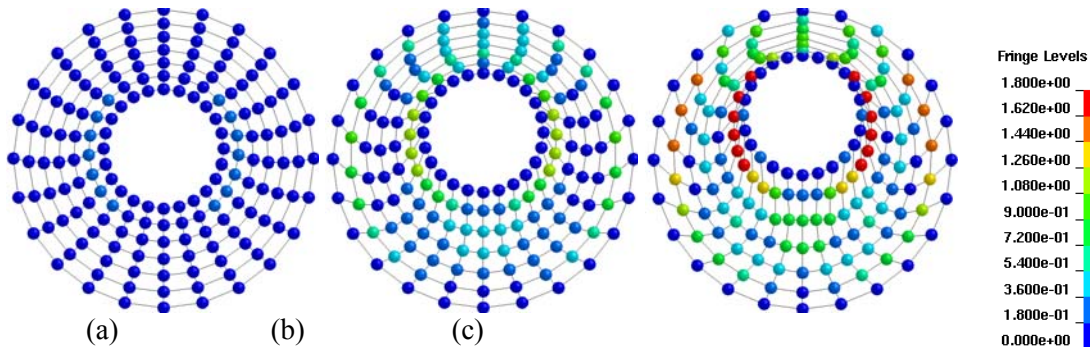


Fig. 5: Progressive deformation with effective plastic strain results by SPG (MLS) method: (a) $d_y = 0.15$, (b) $d_y = 0.45$, and (c) $d_y = 0.75$.

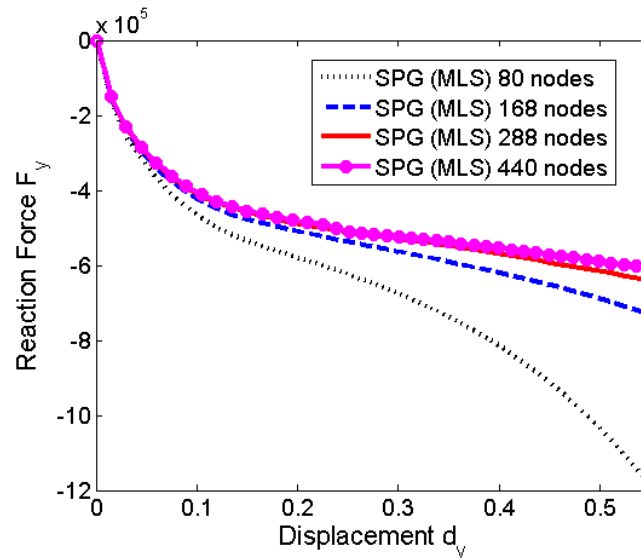


Fig. 6: Convergence study of implicit SPG (MLS) using four discretization refinements.

6.2 3D punch problem

The large deformation problem is studied next in the Prandtl's punch problem using the explicit dynamic analysis. The model is shown in Fig. 7 which consists of a block of size $4 \times 2 \times 1$ punched by a rigid, frictionless and flat plate with a vertical velocity of $v_z = 2.0$. The metal block is assumed elastic and the material properties are: Young's modulus $E = 6.9 \times 10^4$, Poisson's ratio $\nu = 0.3$ and density $\rho_0 = 2.7 \times 10^3$.

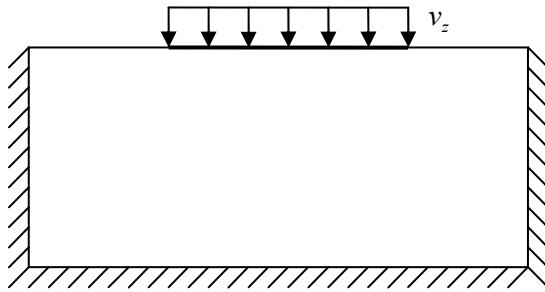


Figure 7: Prandtl's punch model.

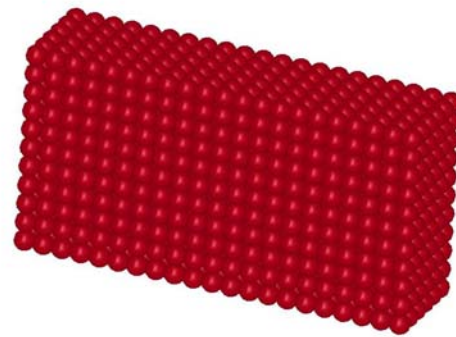


Figure 8: SPG model for punch problem.

The elastic block is discretized by $21 \times 11 \times 5$ uniformly distributed particles as shown in Fig. 8. Cubic spline kernel function with a normalized dilation parameter of 1.6 in X, Y and Z directions is used in the computation. The problem is simulated using both the adaptive Lagrangian kernel approach and Eulerian kernel approach.

Fig. 9 shows the comparison of the deformation plots between the adaptive Lagrangian kernel and Eulerian kernel approach. In the small deformation range, both approaches give almost identical results. However, when the deformation approaches to the large range, they behave quite differently. With the Eulerian kernel, the particles close to the edges of the impacting plate start to lose interaction with each other between $t=0.3$ and 0.4 . This phenomenon leads to a numerical fracture similar to that of tensile instability [12-13] in SPH method and should be avoided. On the other hand, the Lagrangian kernel approach yields smooth and continuous deformation without numerical fracture. To generate a realistic result and prevent any numerical

fracture, a physical-based failure criterion should be employed to both approaches for the consideration in material failure analysis.

It is interesting to show how stable the proposed SPG method is for the 3D large deformation problem. There is no bulk viscosity added in the numerical scheme for this elastic material problem and the computation is finished without shooting nodes or unstable modes.

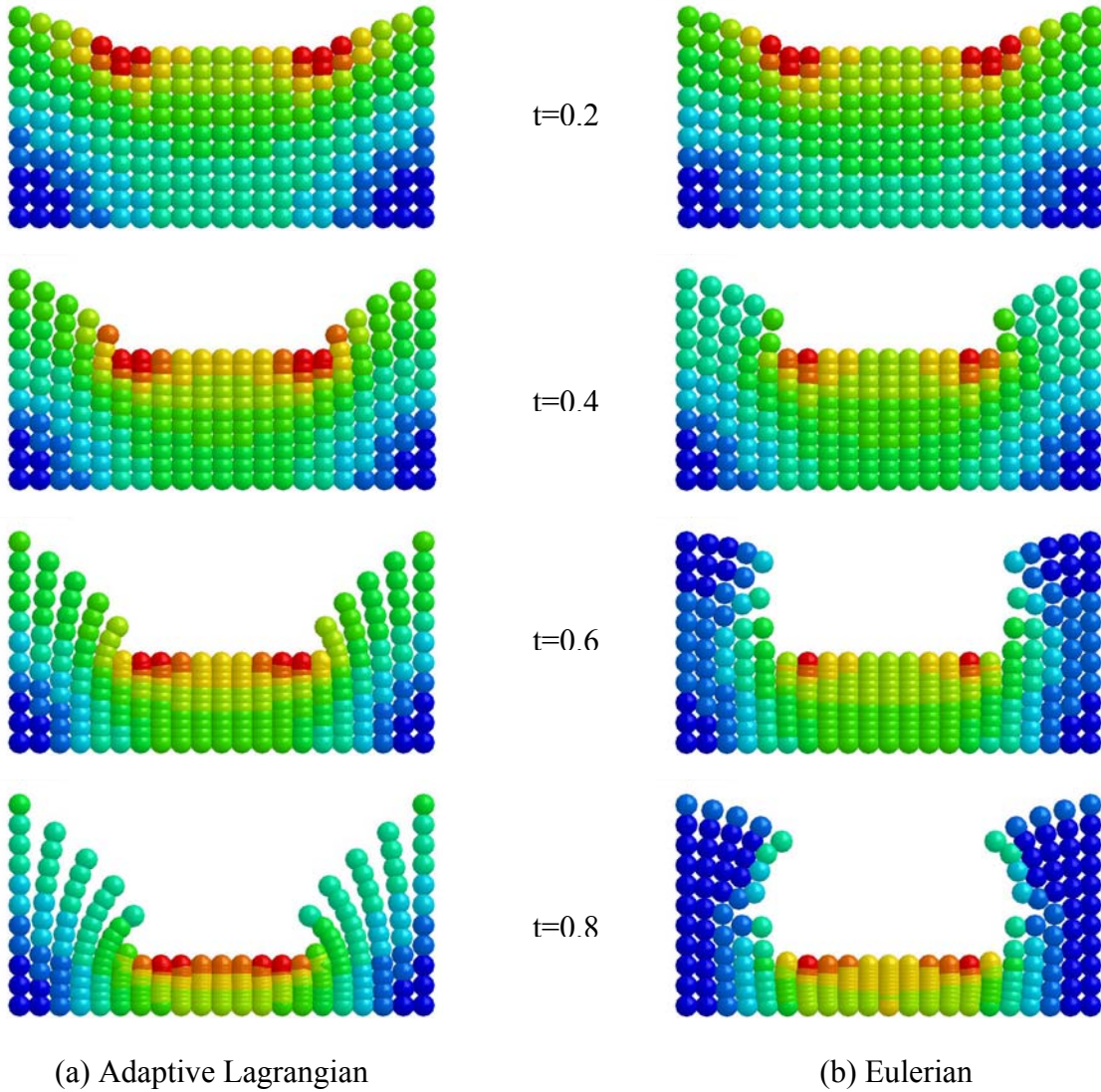


Fig. 9: Progressive deformation with effective von-Mises stress.

6.3 Plate impacted by a rigid ball

The third benchmark problem is a circular plate impacted by a rigid ball, as shown in Fig. 10. The plate has a radius of 20 and a thickness of 5 and is consisted of an elastic-perfectly plastic material with material properties of density $\rho_0 = 7.85 \times 10^{-3}$, Young's modulus $E = 2.0 \times 10^5$, Poisson's ratio $\nu = 0.3$ and yield stress $\sigma_y = 2.0 \times 10^2$. The rigid ball has a radius of 5 and an impact speed of 600.0.

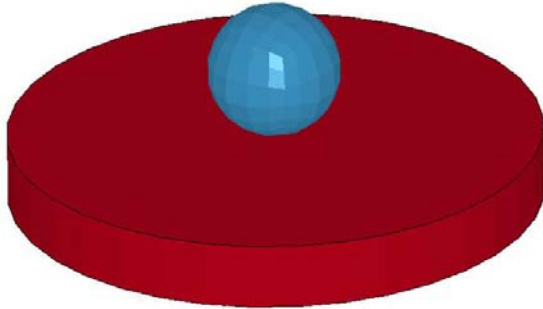


Figure 10: Plate impact by a ball.

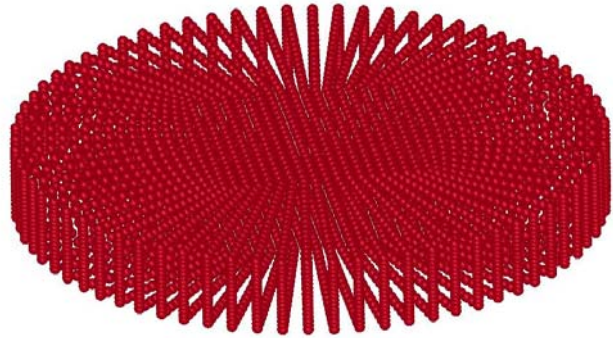


Figure 11: Particle discretization of the plate.

The plate is modeled by 25721 particles as shown in Fig. 11. Cubic spline kernel function with a normalized dilation parameter of 1.6 in X, Y and Z directions is adopted in the computation. To avoid any numerical fracture, the simulation is conducted with the adaptive Lagrangian kernel approach.

The progressive deformation of the plate is plotted in Fig. 14, together with the contours of the effective plastic strain. The results show that the proposed SPG method can handle large deformation with ease. Similar to the previous example, there is no shooting nodes or spurious zero-energy modes observed in the severe deformation range.

The time history of the velocity of the impacting ball and the time history of the impact force are displayed in Figures (12) and (13).

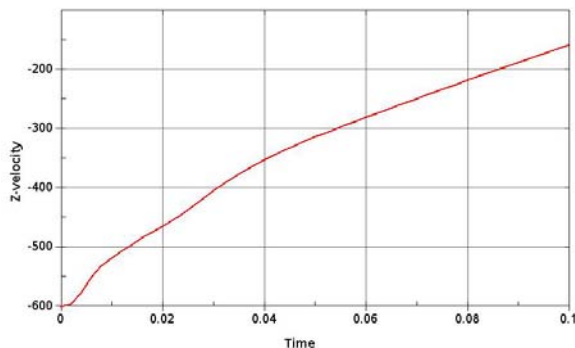


Figure 12: Time history of ball velocity.

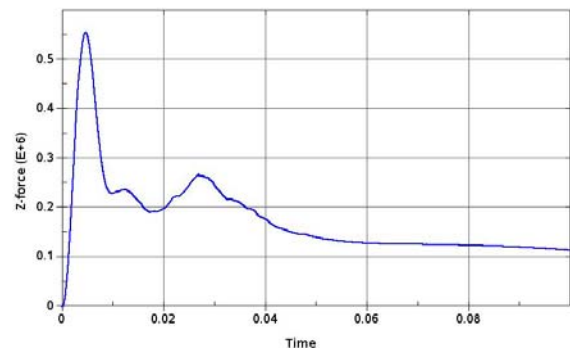


Figure 13: Time history of impact force.

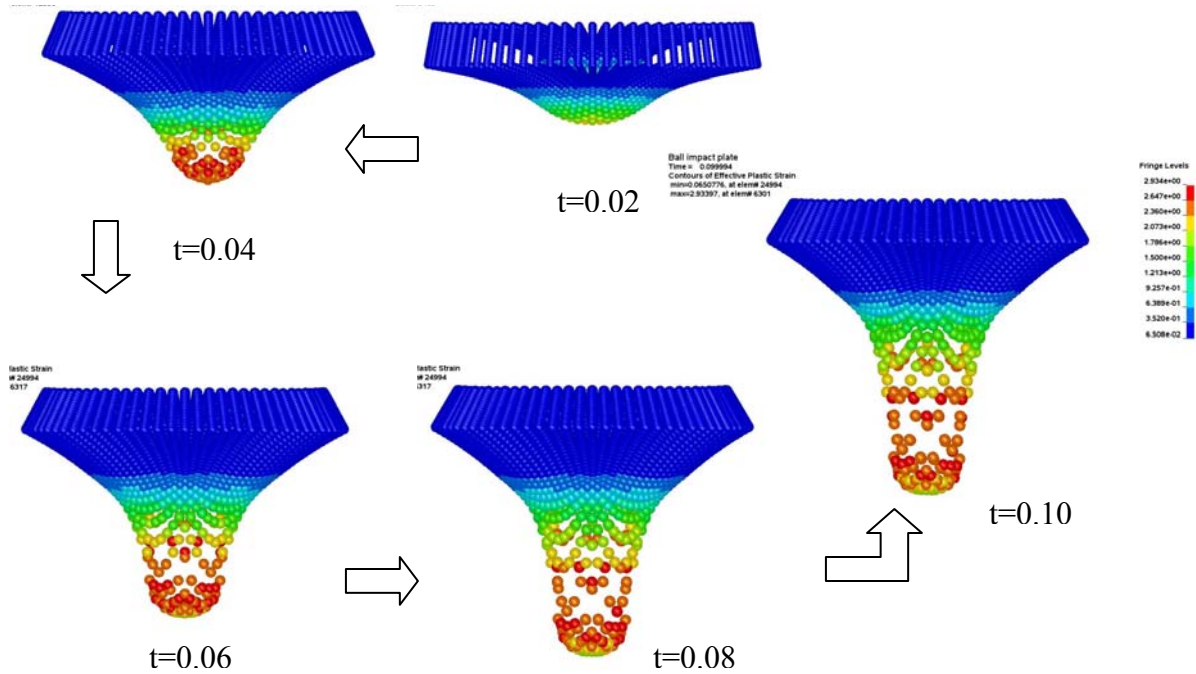


Fig. 14: Progressive deformation of the plate with effective plastic strain.

6.4 Explicit analysis for 3D metal cutting problem

The metal cutting simulation is conducted by the SPG method in this example. The metal block has a size of $4 \times 1 \times 2$ and is subjected to a shear cutting as shown in Fig.15. Same material constants in example 6.1 are used in this example. The cutting speed is 2 unit length/sec and material failure is based on a preset critical strain value. Explicit dynamic analysis and Eulerian kernel approach are performed for this cutting simulation. Under this setting, material will fail before numerical fracture occurs. Since the cutting speed is relatively slow, no buck viscosity is needed in this analysis.

The progress cutting result is plotted in Fig. 16 that displays the effective plastic strain contour. As shown in Fig. 16, no shooting nodes or spurious energy modes are observed in the cutting process. The effective plastic strain distribution is monotonically increased without suffering from the numerical diffusion during the cutting simulation.



Fig. 15: A side view of 3D metal cutting model.

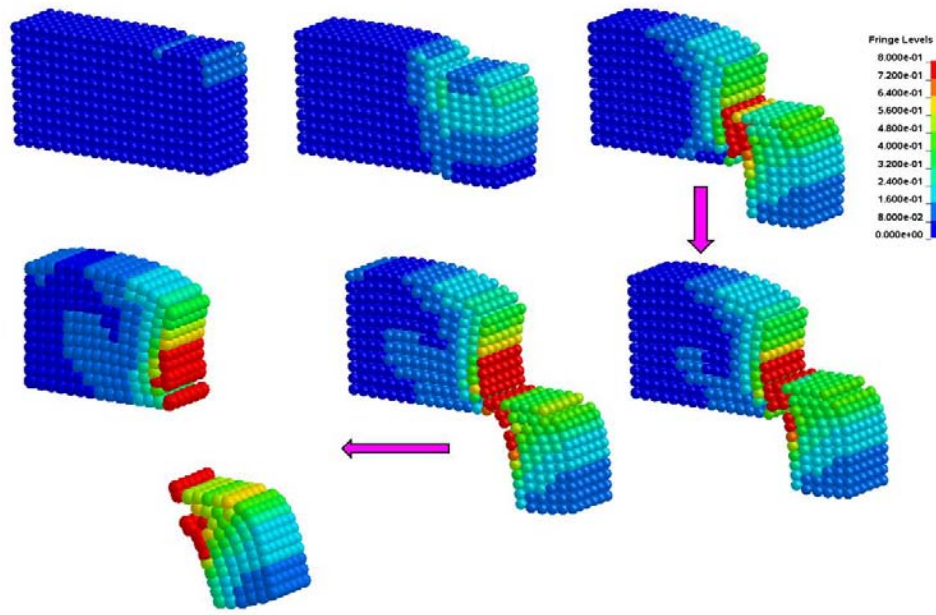


Fig. 16: Progress cutting history plots in effective plastic strain contour.

7. Conclusion

A new particle method is developed for the large inelastic deformation and failure analyses in solid mechanics applications. The present particle method is intimately related to the residual-based stabilization method for the elimination of zero-energy modes in conventional particle methods. No numerical viscosity and artificial control parameters are involved in the present formulation for the stabilization. The numerical results in quasi-static analyses justify the applicability of the present method for the large inelastic deformation analyses. A combination of explicit dynamic formulation and adaptive Lagrangian/Eulerian kernel approach helps advance the simulation to the severe inelastic deformation range. The method also could be a promising alternative for the simulation of impact and penetration problems involving material failure. Its extension to shell formulation is under investigation and will be reported in the near future.

References

- [1] S. Li, W.K. Liu, Meshfree Particle Method, Springer, Berlin 2004.
- [2] C.T. Wu, Y. Guo, E. Askari, Numerical modeling of composite solids using an immersed meshfree Galerkin method, *Composites B* 45 (2013) 1397-1413.
- [3] J.S. Chen, C. Pan, C.T. Wu, W.K. Liu, Reproducing kernel particle methods for large deformation analysis of non-linear structures, *Comput. Methods Appl. Mech. Eng.* 139 (1996) 195-227.
- [4] J. Bonet, S. Kilasegaram, Correction and stabilization of smooth particle hydrodynamics methods with applications in metal forming simulations, *Int. J. Numer. Methods Eng.* 47 (2000) 1189-1214.
- [5] C. Peco, A. Rosolen, M. Arroyo, "An adaptive meshfree method for phase-field models of biomembranes. Part II: A Lagrangian approach for membranes in viscous fluids, *J. Comput. Phys.* 249 (2013) 320-336.
- [6] J.J. Monaghan, An introduction to SPH, *Comput. Phys. Commun.* 48 (1988) 89-96.

- [7] E.S. Lee, C. Moulinec, R. Xu, D. Violeau, Comparisons of weakly compressible and truly incompressible algorithms for the SPH meshfree particle method, *J. Comput. Phys.* 227 (2008) 8417-8436.
- [8] D. Violeau, *Fluid Mechanics and the SPH method: Theory and Applications*, Oxford University Press, Oxford, 2012.
- [9] L.D. Libersky, A.G. Petscheck, T.C. Carney, J.R. Hipp, F.A. Allahadai, High strength Lagrangian hydrodynamics, *J. Comput. Phys.* 109 (1993) 67-75.
- [10] C. T. Wu, W. Hu, M. Koishi, A smoothed particle Galerkin formulation for stabilized large deformation analyses of non-linear continua, submitted to *Journal of Computational Physics* (2014).
- [11] W.K. Liu, S. Jun, Y.F. Zhang, Y. F. Reproducing kernel particle methods, *Int. J. Numer. Methods Fluids* 20 (1995) 1081-1106.
- [12] P.W. Randles, L.D. Libersky, Recent improvements in SPH modeling of hypervelocity impact, *Int. J. Impact Eng.* 48 (2000) 1445-1462.
- [13] J.W. Swegle, D.L. Hicks, S.W. Attaway, Smoothed particle hydrodynamics stability analysis, *J. Comput. Phys.* 116 (1995)123-134.
- [14] T. Belytschko, Y. Guo, W.K. Liu, S.P. Xiao, A unified stability analysis of meshless particle methods, *Int. J. Numer. Methods. Eng.* 48 (2000) 1359-1400.
- [15] T. Rabczuk, T. Belytschko, S.P. Xiao, Stable particle methods based on Lagrangian Kernels, *Comput. Methods Appl. Mech. Eng.* 193 (2004) 1035-1063.
- [16] S. Beissel, T. Belytschko, Nodal integration of the element-free Galerkin method, *Comput. Methods Appl. Mech. Eng.* 139 (1996) 49-74.
- [17] E. Oñate, F. Perazzo, J. Miquel, A finite point method for elasticity problems, *Comput. Struct.* 79 (2001) 2151- 2163.
- [18] J.S. Chen, C.T. Wu, S. Yoon, Y. You, A stabilized conforming nodal integration for Galerkin meshfree methods, *Int. J. Numer. Methods Eng.* 50 (2001) 435-466.
- [19] H.P. Wang, C.T. Wu, Y. Guo, M. Botkin, A Coupled Meshfree/finite Element Method for Automotive Crashworthiness Simulations, *Int. J. Impact Eng.* 36 (2009) 1210-1222.
- [20] C.T. Wu, C.K. Park, J.S. Chen, A generalized approximation for the meshfree analysis of solids, *Int. J. Numer. Methods Engrg.* 85 (2011) 693-722.
- [21] C.K. Park, C.T. Wu, C.D. Kan, On the analysis of dispersion property and stable time step in meshfree method using generalized meshfree approximation, *Finite Elem. Anal. Des.* 47 (2011) 683-697.
- [22] C.T. Wu, W. Hu, Meshfree-enriched simplex elements with strain smoothing for the finite element analysis of compressible and nearly incompressible solids, *Comput. Methods Appl. Mech. Eng.* 200 (2011) 2991-3010.
- [23] C.T. Wu, M. Koishi, Three-dimensional meshfree-enriched finite element formulation for micromechanical hyperelastic modeling of particulate rubber composites, *Int. J. Numer. Methods Eng.* 91 (2012) 1137-1157.
- [24] C.T. Wu, W. Hu, Multi-scale finite element analysis of acoustic waves using global residual-free meshfree enrichments, *Interact. Multiscale Mech.*, 6 (2013) 83-105.
- [25] R. Vignjevic, J. Campbell, L.D. Libersky, A treatment of zero-energy modes in the smoothed particle hydrodynamics method, *Comput. Methods Appl. Mech. Eng.* 184 (2000) 67-85.
- [26] J.C. Simo, T.J.R. Hughes, *Computational Inelasticity*, Springer, New York, 2000.
- [27] *LS-DYNA User's Manual*, Livermore Software Technology Corporation, Livermore, USA, 2013.